



Article

Investigation of High-Q Lithium Niobate-Based Double Ring Resonator Used in RF Signal Modulation

Zhenlin Wu¹, Lin Zhang¹, Shaoshuai Han¹, Di Lian¹, Tongfei Wu¹, Wenjie Chu¹, Haoyu Li¹, Lei Guo², Mingshan Zhao¹  and Xin Yang^{3,*} 

¹ School of Optoelectronic Engineering and Instrumentation Science, Dalian University of Technology, Dalian 116024, China; zhenlinwu@dlut.edu.cn (Z.W.); zhanglin1998@mail.dlut.edu.cn (L.Z.); hanss1224@mail.dlut.edu.cn (S.H.); liandi@mail.dlut.edu.cn (D.L.); wutongfei0125@163.com (T.W.); 18109871393@163.com (W.C.); 1030434749@mail.dlut.edu.cn (H.L.); mszhao@dlut.edu.cn (M.Z.)

² School of Information and Communication Engineering, Dalian University of Technology, Dalian 116024, China; leiguo@dlut.edu.cn

³ Department of Electrical and Electronics Engineering, School of Engineering, Cardiff University, Cardiff CF10 3AT, UK

* Correspondence: yangx26@cardiff.ac.uk

Abstract: In recent years, millimeter-wave communication has played a crucial role in satellite communication, 5G, and even 6G applications. The millimeter-wave electro-optic modulator is capable of receiving and processing millimeter-wave signals effectively. However, the large attenuation of millimeter waves in the air remains a primary limiting factor for their future applications. Therefore, finding a waveguide structure with a high quality factor (Q-factor) is critical for millimeter-wave electro-optic modulators. This manuscript presents the demonstration of a double ring modulator made of lithium niobate with the specific goal of modulating an RF signal at approximately 35 GHz. By optimizing the microring structure, the double ring resonator with high Q-factor is studied to obtain high sensitivity modulation of the RF signal. This manuscript employs the transfer matrix method to investigate the operational principles of the double ring structure and conducts simulations to explore the influence of structural parameters on its performance. Through a comparison with the traditional single ring structure, it is observed that the Q-factor of the double ring modulator can reach 7.05×10^8 , which is two orders of magnitude greater than that of the single ring structure. Meanwhile, the electro-optical tunability of the double ring modulator is 6 pm/V with a bandwidth of 2.4 pm, which only needs 0.4 V driving voltage. The high Q double ring structure proposed in this study has potential applications not only in the field of communication but also as a promising candidate for a variety of chemical and biomedical sensing applications.

Keywords: ring resonator; lithium niobate; high quality factor; RF signal; modulation



Citation: Wu, Z.; Zhang, L.; Han, S.; Lian, D.; Wu, T.; Chu, W.; Li, H.; Guo, L.; Zhao, M.; Yang, X. Investigation of High-Q Lithium Niobate-Based Double Ring Resonator Used in RF Signal Modulation. *Appl. Sci.* **2023**, *13*, 4648. <https://doi.org/10.3390/app13074648>

Academic Editor: Edik U. Rafailov

Received: 12 March 2023

Revised: 31 March 2023

Accepted: 3 April 2023

Published: 6 April 2023



Copyright: © 2023 by the authors. Licensee MDPI, Basel, Switzerland. This article is an open access article distributed under the terms and conditions of the Creative Commons Attribution (CC BY) license (<https://creativecommons.org/licenses/by/4.0/>).

1. Introduction

As a key device of photon integrated circuits (PICs), the microring resonator (MRR) [1,2] shows excellent performance in filtering [3], sensing [4,5], high-speed electric-optical modulation [6,7], generation of optical frequency comb [8], and wavelength division multiplex (EDM) [9,10] due to its unique properties, such as wavelength selectivity, compactness, and high Q-factor. Over the past few decades, electro-optic modulator (EOM) composed of MRR has been extensively studied in various material systems, including graphene [11], silicon (Si) [12], lithium niobate (LN) [13,14], indium phosphide (InP), and polymers [15]. These materials have their own advantages, but there are still some limiting factors for their application. The development of Si and InP modulators for ultrahigh speed data transmission will be limited as they depend on plasma dispersion effect and the quantum local Stark effect, respectively. The problem with graphene is that its monolayer structure is technically difficult to be separated; it cannot be mass-produced [14]; even though electro-optic polymers

have shown very high electro-optic coefficients, this coefficient will gradually decrease as the material ages, leading to less effective stability.

Lithium niobate is an artificially synthesized material that possesses remarkable electro-optical, acoustic, piezoelectric, and nonlinear optical properties, as well as outstanding transmittance [16] in the near-infrared spectral range. The lithium niobate on insulators (LNOI) platform has been extensively studied for the fabrication of various waveguide structures, including LN waveguides [17], proton-exchanged waveguides [18], and strip-loaded waveguides [19]. Due to the higher electric-optical coefficient of LN ($\gamma_{33} = 31$ pm/V) and large refractive indices, EOM based on LN material has developed rapidly in recent years. Several hybrid waveguide modulators have been proposed, including Si/LiNbO₃ and Si₃N₄/LiNbO₃ [20]. As the LN material has been recognized as difficult to etch, its fabrication technology has been studied for years. In 2017, Mian Zhang et al., at Harvard University, developed the optimized standard etching process to prepare LN waveguides with propagation loss as low as 2.7 ± 0.3 dB/m. In 2018, Wu et al. reported a LN waveguide with propagation loss as low as 2.7 dB/m by using a chemical mechanical polishing method [21]. In recent years, the use of lithium niobate in the field of optics has attracted increasing attention [22,23]. After careful consideration of various factors, including the advancement in lithium niobate etching processes, we ultimately selected lithium niobate as the waveguide material.

In this paper, a high-sensitivity electro-optical modulator for 35 GHz satellite communication is designed, and the structural parameters and ideal performance of the double ring modulator are determined by using FDTD. The structural coefficients that fundamentally affect the performance of the double ring structure, such as transmission coefficient and transmission loss, are exhaustively studied by the transmission matrix method. The optimized double ring structure can achieve a Q-factor that is two orders of magnitude higher than that of the single ring structure, and its application in 35 GHz communication can achieve higher modulation sensitivity. Compared with other devices used in the field of high frequency RF modulation, it has the characteristics of higher sensitivity and integration. Ultimately, the optimized double ring structure with excellent performance has a very broad application potential in the field of communication and biochemical sensing.

2. Materials and Methods

The schematic structure of the waveguide and the substrate is shown in Figure 1a. The underlying substrate is 0.5 mm thick silicon with a coating layer of 2 μ m thick silicon dioxide. The core layer is composed of 600 nm thick x-cut LN film. Lumped gold electrodes deposited on the left and right sides of the inner ring waveguide are used to apply RF signals. In order to prevent external dust, water vapor, and other pollutants from affecting the performance of the structure, a layer of SiO₂ is deposited on the top to enhance the stability of the device. The light of 1550 nm is used as the carrier wavelength and the refractive indices of the waveguide are $n_e = 2.138$, $n_o = 2.211$, and $n_{\text{SiO}_2} = 1.444$, which possess a large core-envelope refractive index difference of the LNOI structure ($\Delta n > 0.7$), providing strong light field restriction of the proposed waveguide. The outer ring adopts the add-drop structure. By optimizing the dimensions of the waveguide cross section, bending radius, upper coating thickness, electrode spacing, and other parameters, the insertion loss of the transmitted light can be minimized. For the light induced into the inner ring resonator, it will meet its resonant conditions and start to oscillate, which will help to enhance the interaction with the electric field and achieve higher modulation efficiency. The transmission parameters of the double ring modulator are shown in Figure 1b, which consists of waveguide length (L), intensity of light field (E), transmission coefficient (t), and coupling coefficient (k).

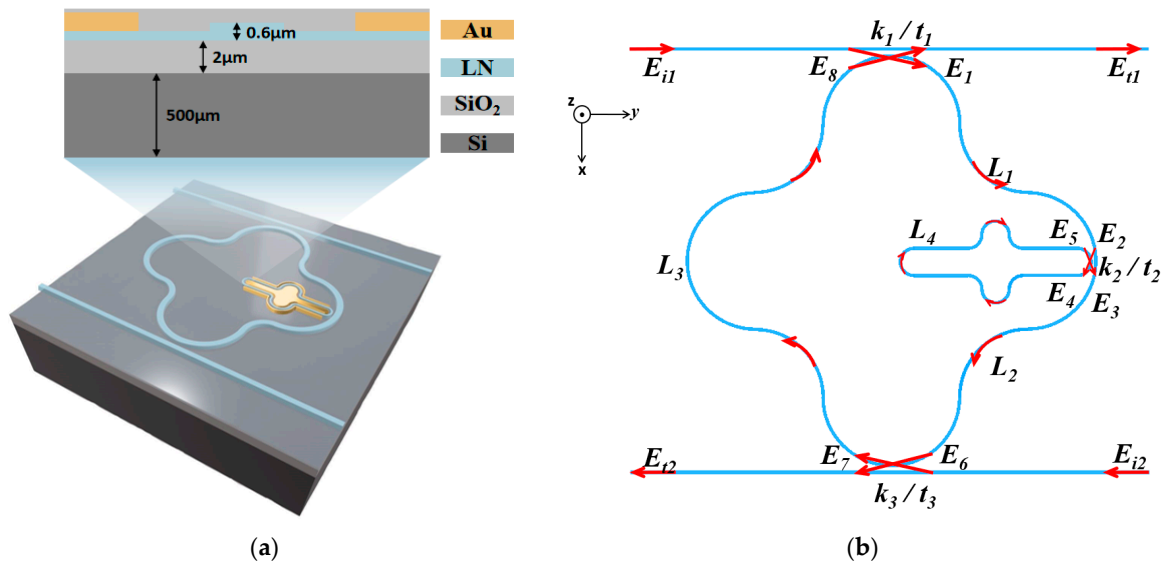


Figure 1. (a) Schematic diagram of the structure of the double ring modulator, where the enlarged area is a cross-section view of the devices. (b) Parameter distribution in the schematic diagram of double ring structure, including transmission coefficient (t), coupling coefficient (k), waveguide length (L), and the intensity of light field (E).

Assuming that the amplitude of incident light is E_{i1} in the case of no coupling loss, the transmission characteristics of the three coupling regions can be obtained by using the transmission matrix method, and the matrix relationship among the coupling regions can be expressed as in Equations (1)–(3);

$$\begin{bmatrix} E_{t1} \\ E_1 \end{bmatrix} = \begin{bmatrix} t_1 & jk_1 \\ jk_1 & t_1 \end{bmatrix} \begin{bmatrix} E_{i1} \\ E_8 \end{bmatrix} \tag{1}$$

$$\begin{bmatrix} E_{t2} \\ E_7 \end{bmatrix} = \begin{bmatrix} t_3 & jk_3 \\ jk_3 & t_3 \end{bmatrix} \begin{bmatrix} E_{i2} \\ E_6 \end{bmatrix} \tag{2}$$

$$\begin{bmatrix} E_3 \\ E_4 \end{bmatrix} = \begin{bmatrix} t_2 & jk_2 \\ jk_2 & t_2 \end{bmatrix} \begin{bmatrix} E_2 \\ E_5 \end{bmatrix} \tag{3}$$

where t and k represent the transmission and coupling coefficients of the coupling regions, and the relationship between these two parameters is: $|t|^2 + |k|^2 = 1$. When add port has no add input ($E_{i2} = 0$), the transmission relationship between different coupling regions can be expressed by Equations (4)–(7);

$$E_2 = e^{-\rho L_1} e^{j\theta_1} E_1 \tag{4}$$

$$E_6 = e^{-\rho L_2} e^{j\theta_2} E_3 \tag{5}$$

$$E_8 = e^{-\rho L_3} e^{j\theta_3} E_7 \tag{6}$$

$$E_5 = e^{-\rho L_4} e^{j\theta_4} E_4 \tag{7}$$

where ρ is the loss coefficient of the microring, L_i ($i = 1,2,3,4$) is the length of each part of the microring, and θ_i ($i = 1,2,3,4$) is the phase change over the corresponding length L_i . The final transmission equation of the through port can be obtained through the normalization of the light field amplitude at each port, as shown in Equation (8):

$$\frac{E_{t1}}{E_{i1}} = t_1 + \frac{-k_1^2 t_2 t_3 e^{-\rho(L_1+L_2+L_3)+j(\theta_1+\theta_2+\theta_3)} + k_1^2 t_2^2 t_3 e^{-\rho(L_1+L_2+L_3+L_4)+j(\theta_1+\theta_2+\theta_3+\theta_4)} + k_1^2 k_2^2 t_3 e^{-\rho(L_1+L_4)+j(\theta_1+\theta_4)}}{1 - t_2 e^{-\rho L_4+j\theta_4} - t_1 t_2 t_3 e^{-\rho(L_1+L_2+L_3)+j(\theta_1+\theta_2+\theta_3)} + t_1 t_2^2 t_3 e^{-\rho(L_1+L_2+L_3+L_4)+j(\theta_1+\theta_2+\theta_3+\theta_4)} + t_1 k_2^2 t_3 e^{-\rho(L_1+L_4)+j(\theta_1+\theta_4)}} \quad (8)$$

Using the same method, the transmission equation of the through port of single ring resonator can be obtained, as in Equation (9):

$$\frac{E_{t1}}{E_{i1}} = \frac{t_2 - t_2 e^{-\rho L_4+j\theta_4}}{1 - t_2^2 e^{-\rho L_4+j\theta_4}} \quad (9)$$

The transmission spectra of the double ring and single ring resonators can be plotted based on Equations (8) and (9), as illustrated in Figure 2. Since the inner ring of the double ring structure is equivalent to increase the virtual length of the outer ring, which increases the length of the optical field reacting with the waveguide, the double ring structure achieves resonance enhancement. This eventually makes the resonance peak of the double ring resonator much sharper than that of the single ring resonator. The Q-factor of the double ring resonator can reach 7.05×10^8 , which is two orders of magnitude higher than that of the single ring resonator. The high Q-factor plays a crucial role in facilitating efficient interaction between the optical and electric fields, ultimately resulting in improved electro-optic tunability of the device.

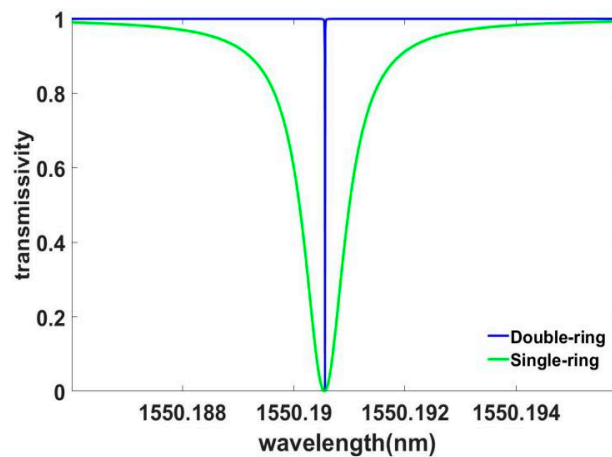


Figure 2. Comparison of resonant peaks of double ring resonator and single ring resonator at the same resonant wavelength. The ring length of the single ring resonator is the same as the inner ring length of the double ring resonator.

3. Results and Discussion

3.1. Optimization Design of the Waveguide Parameters

To realize low loss and efficient transmission of optical carrier, the dimensions of the waveguide cross section and bending radius of the waveguide are optimized. The ridge-type waveguide structure can effectively reduce the scattering loss as this structure can reduce the light interaction with the sidewalls. In this work, the proposed device adopts this structure. The total thickness of lithium niobate film is 600 nm, in which the thickness of residual layer is 250 nm and the ridge height is 350 nm. Figure 3a shows the single-mode condition of the waveguide. The critical points of single-mode of both TE and TM modes can be found at $w = 1 \mu\text{m}$ and $0.8 \mu\text{m}$, respectively. Figure 3b,c show that with gradually increasing waveguide width (w), the waveguide transmission loss decreases and the optical power propagated in LN layer increases. The higher proportion of light field confined in LN, the greater the opto-electric overlap factor will be, causing the modulator to have higher electro-optic modulation efficiency. Figure 3e shows that with the increase of the electrode spacing, the absorption of the waveguide gradually decreases, resulting in a gradual decrease of waveguide loss. Finally, the dimensions of the waveguide are also

determined. As shown in Figure 3a, the waveguide width is chosen to be 0.8 μm in order to guarantee the single-mode condition. In this case, the effective refractive index (n_{eff}) is 1.85, and the group refractive index (n_g) is 2.23. It can be seen from Figure 3c that with 0.8 μm waveguide width, the optical power ratio in LN waveguide exceeds 80%. It can be noticed from Figure 3d that when the bending radius is greater than 100 μm , the waveguide loss is approximately equal to that of the straight waveguide and tends to be stable. Therefore, the bending radius of 100 μm is chosen in our design. The electrode spacing of 6 μm is selected for a lower insertion loss.

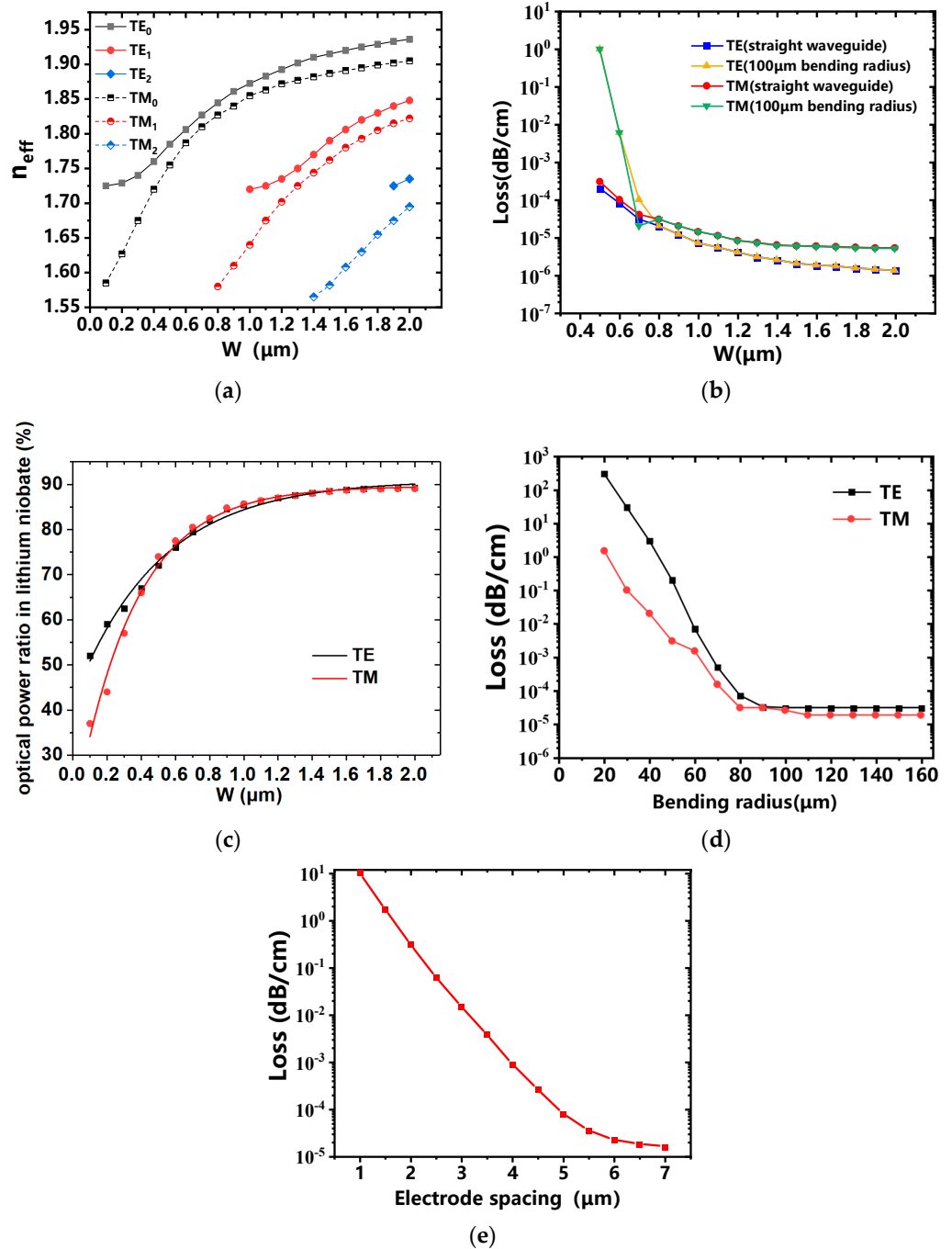


Figure 3. (a) The effective refractive index at different waveguide width; (b) the waveguide loss at different waveguide width; (c) the optical power ratio in lithium niobate at different waveguide width; (d) the waveguide loss at different bending radius; and (e) the transmission loss of the LN waveguide with different electrode spacing.

3.2. Modulation Mechanism of the Microring Resonator

As shown in Figure 4a, the working principle of the lumped electro-optic modulator is that when the radio frequency field incidents into the microring resonator of LNOI, the refractive index of the LN crystal varies linearly with the electric field intensity due to the Pockels effect, resulting in the drift of the microring transmission spectrum, and finally changing the output light intensity. Figure 4b shows that when the optical carrier with the frequency of f_{opt} is modulated by the RF electric field, two sidebands of different frequencies will be generated near the optical carrier with the frequency of $f_{opt} - f_{RF}$ and $f_{opt} + f_{RF}$. Free Spectral Range (FSR) is the distance between adjacent resonant peaks, which is one of the key parameters of microring resonator. To observe the change of the output light intensity, the two sidebands should fall within the microring resonance peak; that is, conditions $f_{RF} = m \cdot f_{FSR}$ ($m = 1, 2, 3 \dots$) or $f_{RF} < f_{FWHM}$, where f_{FWHM} is the full width of the resonant peak. The second condition ($f_{RF} < f_{FWHM}$) is suitable for low-frequency signal modulation, but the target RF signal of the modulator designed in this paper is 35 GHz, so the condition $f_{RF} = m \cdot f_{FSR}$ should be satisfied. It is noteworthy that the input light needs to be placed at the maximum slope of the resonant peak. In this case, even if the received RF signal is very weak, the modulation light intensity will change greatly.

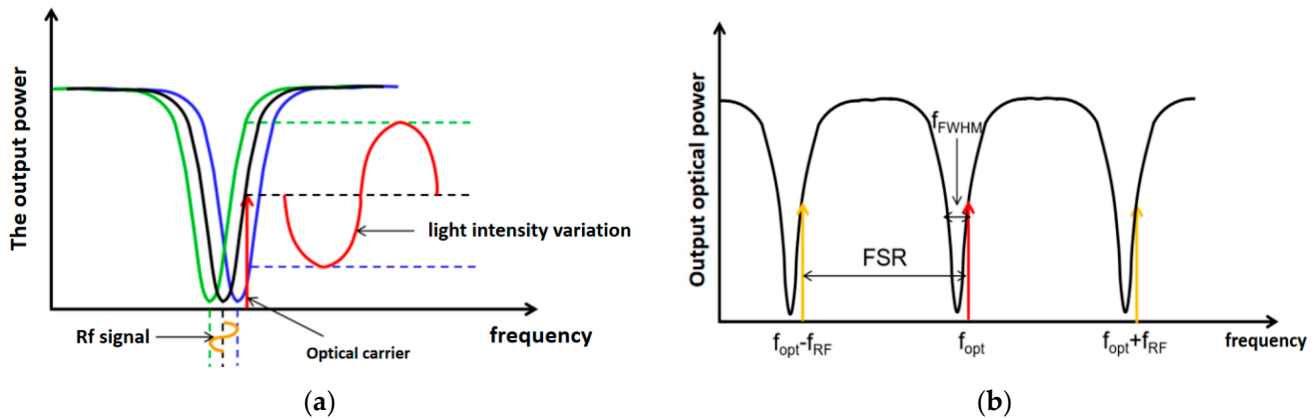


Figure 4. (a) Intensity modulation of the microring resonator. The green, black and blue lines show the drift of the resonant wavelength of the material in the microring modulator due to the pockels effect due to the change in RF signal, and the red line shows the change in light intensity as the RF signal is modulated onto the light. (b) Mechanisms for setting the parameters of the microring resonator. The red line is the local oscillation light and the yellow line is the sideband of the modulated finished RF signal, which carries the RF information.

The relationship between FSR and the length of the microring can be expressed as in Equation (10);

$$f_{FSR} = \frac{\lambda^2}{L \cdot n_g} \tag{10}$$

where L is the total length of microring, n_g is group refractive index, and λ is optical carrier wavelength. Given the values of n_g and λ , the length L can be derived by Equation (10), which yields a result of 3846.6 μm . This corresponds to the microring length for a 35 GHz RF modulator.

Figure 5 shows that when transmission loss is not taken into account, the maximum Q-factor is reached when the length of the outer ring is twice that of the inner ring. Considering the factors of the integration of the chip and the improvement of sensitivity, the parameters will be discussed and analyzed below when the outer ring length as twice the inner ring.

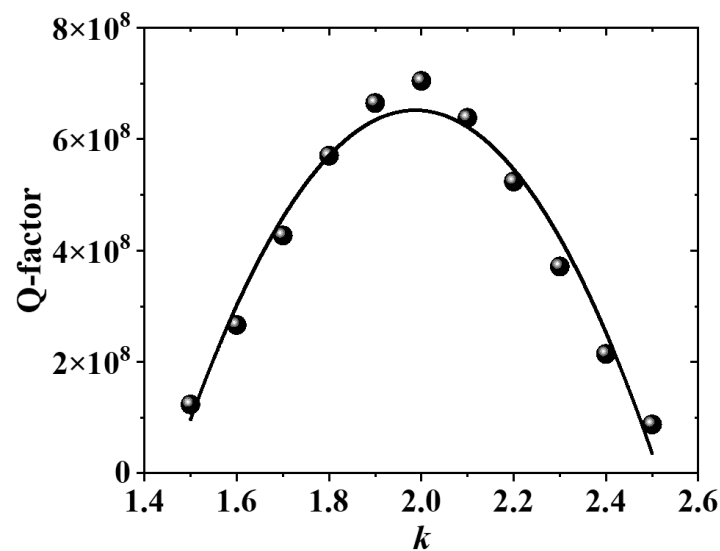


Figure 5. The Q-factor of resonator with the ratio (k) of outer ring length to inner ring length.

3.3. Analysis of Double Ring Structure

Assuming no waveguide loss under the analysis and comparison of the coupling coefficients k_1, k_2, k_3 on the transmission characteristics of the double ring resonator, as shown in Figure 6. Figure 6a shows that with $k_1 = 0.1$, the Q-factor and extinction ratio of the inner ring resonance peak gradually decrease as k_2 and k_3 gradually increase, and the inner ring resonance peak drifts toward the longer wavelength. Figure 6b shows that with $k_2 = k_3 = 0.1$, k_1 gradually increases, and the extinction ratio of the inner ring resonance peak gradually decreases, but the resonant peak does not drift apparently. Figure 6c shows that with $k_2 = 0.1$, k_1 and k_3 increase gradually at the same time, and the position and extinction ratio of the inner ring resonance peak do not change significantly, but the Q-factor of the resonance peak decreases accordingly. By comparing Figure 6a–c, it can be concluded that in the preparation process, if the two gaps of the straight and curved waveguides are different, the coupling coefficients will be different, which destroys the resonance enhancement of the double ring and thus affects the critical coupling state. Figure 6d shows that in the case of $k_1 = k_2 = 0.1$, with the gradual increase of k_3 , the extinction rate of the resonant peak of the inner ring does not change significantly, but the position of the resonant peak drifts toward the longer wavelength and the Q-factor decreases. Based on the above discussion, it is concluded that since a smaller coupling coefficient leads to a smaller bandwidth of light being coupled into the microring, making the resonant enhancement of light at specific wavelengths more intense, resulting in a high Q-factor. Therefore, it is necessary to ensure a smaller coupling coefficient in the structural design and a higher precision in the coupling region during the chip fabrication to obtain a high Q-factor of the device.

When the waveguide loss of the microring is considered, the greater the loss, the worse the transmission characteristics of the microring. The field attenuation of outer ring and inner ring for one round trip are characterized by A_1 and A_2 , respectively, and the relation between the transmission loss ρ and the field attenuation is $A = e^{-\rho L}$. Figure 7a shows that in the case of no loss in the inner ring, the Q-factor and extinction ratio of the double ring resonant peak gradually decrease with the reduction of A_1 . Figure 7b shows that with no loss in the outer ring, the resonance peak of the inner ring deteriorates significantly with the continuous reduction of A_2 . This result reveals that the transmission loss of the microring has a great impact on the performance of the modulator. As LN is recognized as a difficult material to be etched, large losses will inevitably be introduced in the actual preparation process of the waveguide, it is important to determine the critical coupling conditions to remedy this problem.

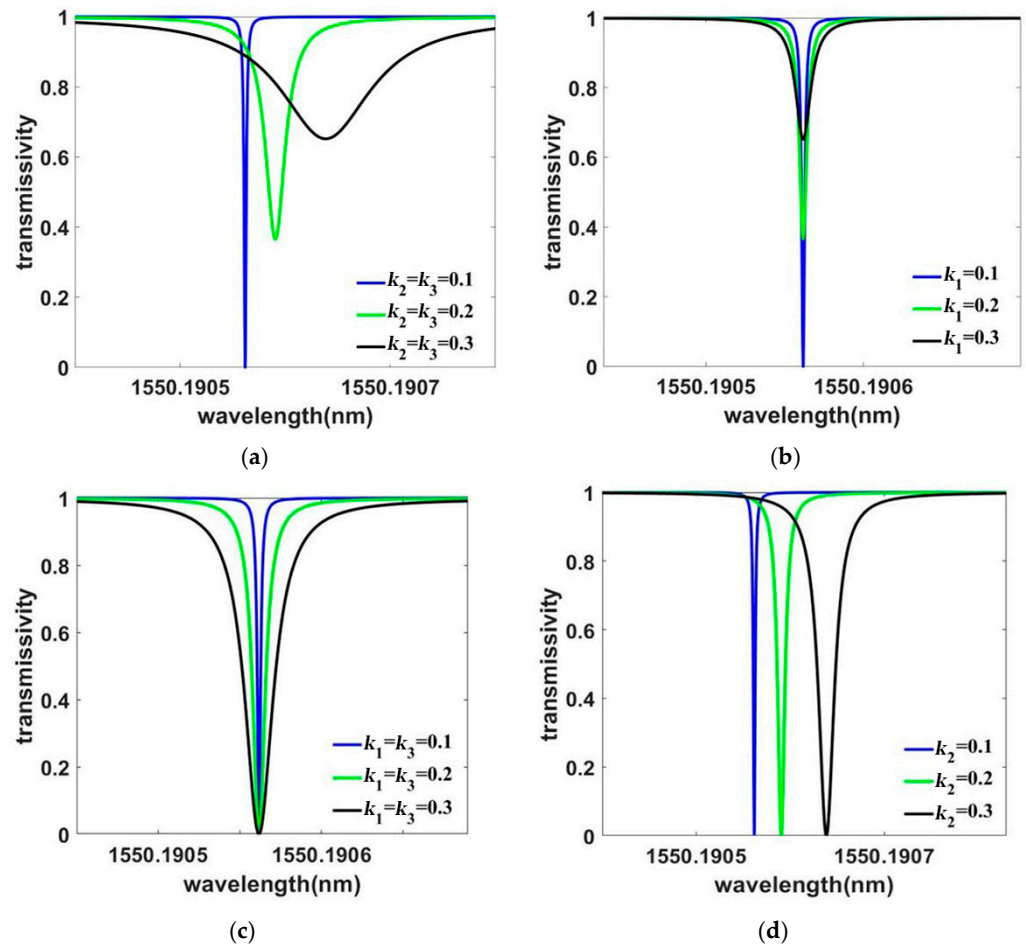


Figure 6. (a) The transmissivity of the double ring resonator at different wavelengths and coupling coefficients (k_2, k_3); (b) the transmissivity of the double ring resonator at different wavelengths and coupling coefficients (k_1); (c) the transmissivity of the double ring resonator at different wavelengths and coupling coefficients (k_1, k_3) and (d) the transmissivity of the double ring resonator at different wavelengths and coupling coefficients (k_2). All other unchanged coupling coefficients are fixed at 0.1.

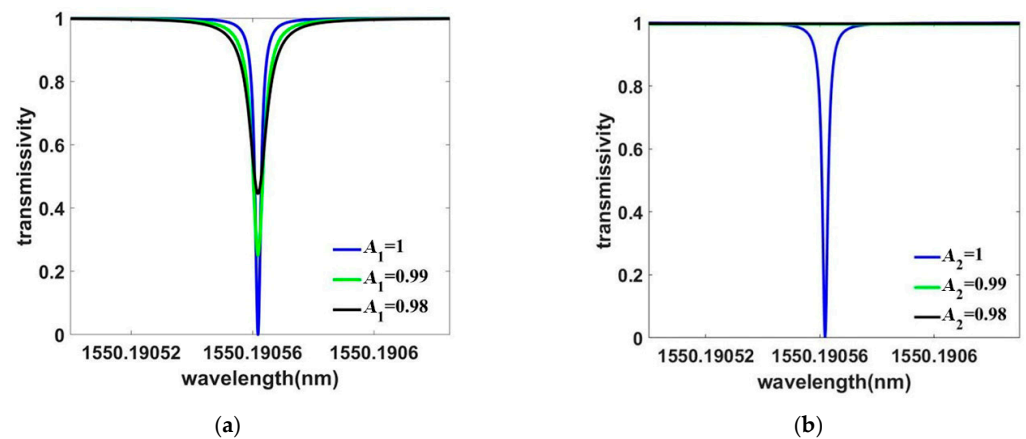


Figure 7. (a) The transmissivity of the double ring resonator at different wavelengths and the field attenuation of outer ring (A_1) and (b) the transmissivity of the double ring resonator at different wavelengths and the field attenuation of inner ring (A_2). Both are calculated at $k_1 = k_2 = k_3 = 0.1$.

When it meets the critical coupling condition, the output power of the through port drops to zero. At this time, the relationship between transmission coefficient and transmission loss is shown in Equation (11).

$$t_1 = t_3 A_1 \left| \frac{t_2 - A_2}{1 - t_2 A_2} \right| \tag{11}$$

Figure 8a shows that with the value of A_1 decreases from 1 to 0.98, the power of input light coupled into the outer ring resonator decreases by about 35%, and the Q-factor of the resonant peak of the inner ring decreases by an order of magnitude. Figure 8b shows that without waveguide loss in the inner ring, the influence of the outer ring waveguide loss on the transmission characteristics is insignificant; the inner ring waveguide loss has a greater influence on the transmission spectrum than that of the outer ring. Figure 9 shows the influence of the transmission coefficients of ring-ring waveguide (t_2) and ring-straight waveguide (t_3) on the transmission spectrum of the double ring resonator. Figure 9a shows that with the transmission coefficient increasing from 0.7 to 0.9, the optical power coupled into the outer ring resonator decreases by about 18%. It is helpful to reduce the interference of outer ring to inner ring transmission characteristics. Figure 9b shows that compared with t_3 , the increase of t_2 will offset the resonance peak of the outer ring, but the effect on the Q-factor of the inner ring is not as obvious as that of t_3 .

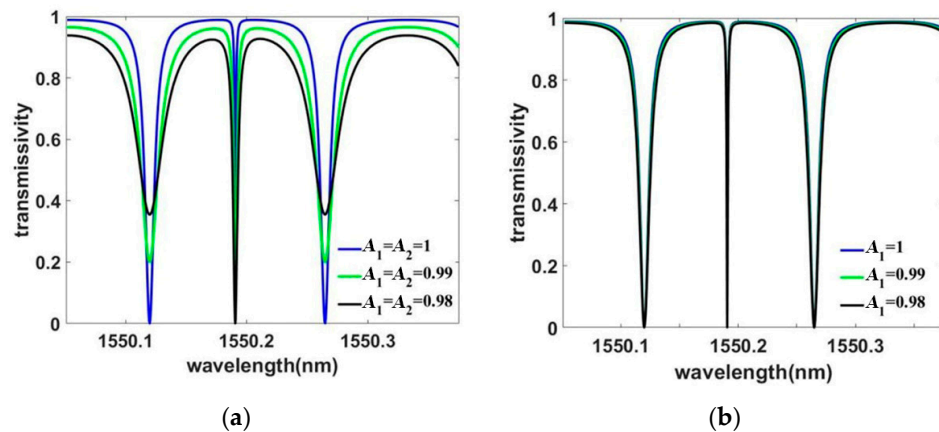


Figure 8. (a) The transmissivity of the double ring resonator at different wavelengths and the field attenuation ($A_1 = A_2$) and (b) the transmissivity of the double ring resonator at different wavelengths and the field attenuation of outer ring (A_1). Both are calculated at $t_2 = t_3 = 0.9$. The resonance peak in the middle is the inner ring resonance peak, and the resonance peak on both sides is the outer ring resonance peak.

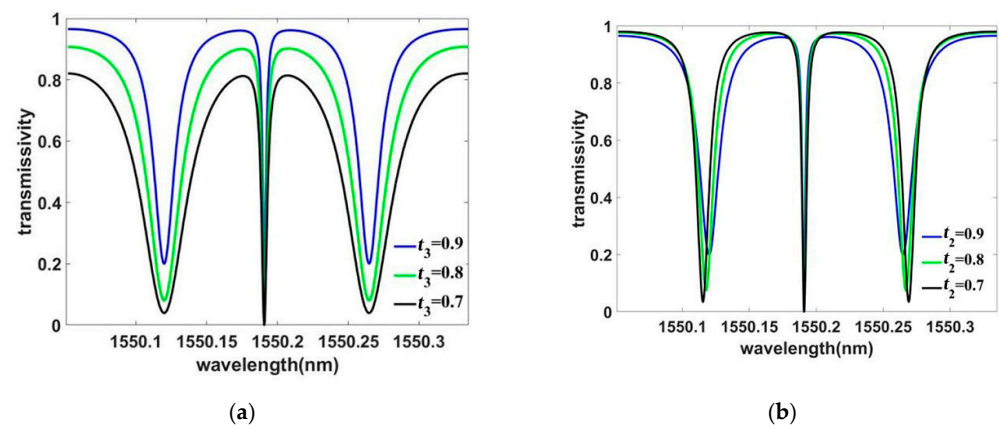


Figure 9. (a) The transmissivity of the double ring resonator at different wavelengths and the transmission coefficient (t_3) and (b) the transmissivity of the double ring resonator at different wavelengths and the transmission coefficient (t_2). Both are calculated at $A_1 = A_2 = 0.99$.

3.4. Double Ring Electro-Optic Modulator

After the analysis of the waveguide loss, characteristic parameters of the coupling region and critical coupling conditions, the modulator with high electro-optic modulation efficiency can be designed according to the factors that affect the performance of the double ring resonator. To analyze differences between double ring resonator and single ring resonator, the parameters are determined as $\rho = 3 \text{ dB/m}$, $t_2 = 0.9$, $t_3 = 0.995$, $t_1 = 0.779$ and the resonator satisfies the critical coupling condition. The simulation result is shown in Figure 10. The single ring resonator has a Q-factor of 6.2×10^4 , and 23% of its light is confined to resonating in the microring. The double ring resonator has a Q-factor of 6.5×10^5 , FWHM = 2.4 pm (300 MHz), FSR = 35 GHz and almost all of the light is confined to resonating in the inner ring. Figure 11 shows the relationship between coupling coefficient and coupling gap in the coupling region between straight–ring waveguide and ring–ring waveguide. The coefficients of the coupling region are determined: $t_1 = 0.779$, $t_2 = 0.9$ and $t_3 = 0.995$, the corresponding gap parameters are $Gap_1 = 565 \text{ nm}$, $Gap_2 = 520 \text{ nm}$ and $Gap_3 = 1205 \text{ nm}$.

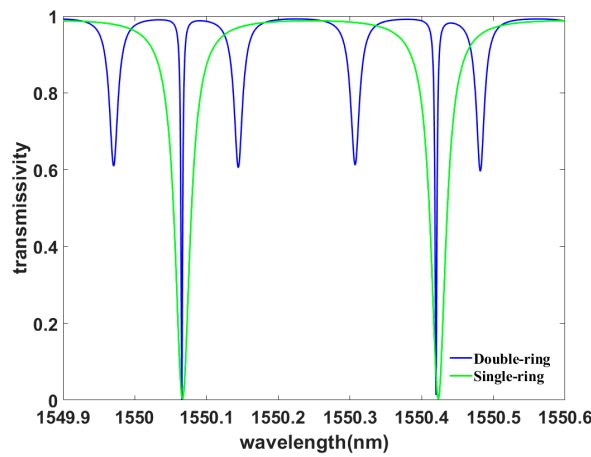


Figure 10. Transmission characteristic curves of the single ring (green line) and the double ring (blue line) resonators at $\rho = 3\text{dB/m}$, $t_2 = 0.9$, $t_3 = 0.995$, $t_1 = 0.779$.

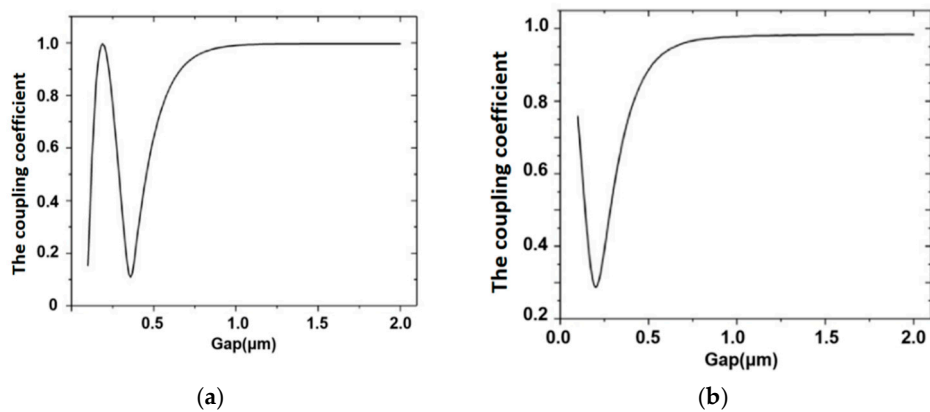


Figure 11. (a) The coupling coefficient of the coupling region of the straight-ring waveguide at different coupling gap and (b) the coupling coefficient of the coupling region of the ring–ring waveguide at different coupling gap.

With 35 GHz RF signal applied to the electrodes, the electric field generated between the electrodes will change the refractive index of LN, which will shift the transmission spectrum of the microring. This eventually results in output light intensity change. The

applied RF signal and the effective refractive index n_{eff} of the waveguide can be represented by Equation (12):

$$n'_{eff} = n_{eff} - \frac{1}{2d} n_{eff}^3 \gamma_{33} \Gamma \bar{V} \quad (12)$$

$$\bar{V} = \frac{2}{T} V \int_0^{\frac{T}{2}} \sin\left(\frac{2\pi}{T} t\right) dt = \frac{2V}{\pi} \quad (13)$$

where d is the electrode spacing, Γ is an electric-optical overlap factor; its value is 0.7, and \bar{V} is the average voltage applied on the electrode as shown in Equation (13), where V is the peak voltage of the input RF signal.

Figure 12a shows the relationship between the transmission characteristic curves of the double ring resonator and the applied voltage V . Figure 12b shows the drift of resonant peak under different applied voltages, and the electro-optic tunability of the double ring resonator is 6 pm/V by linear fitting.

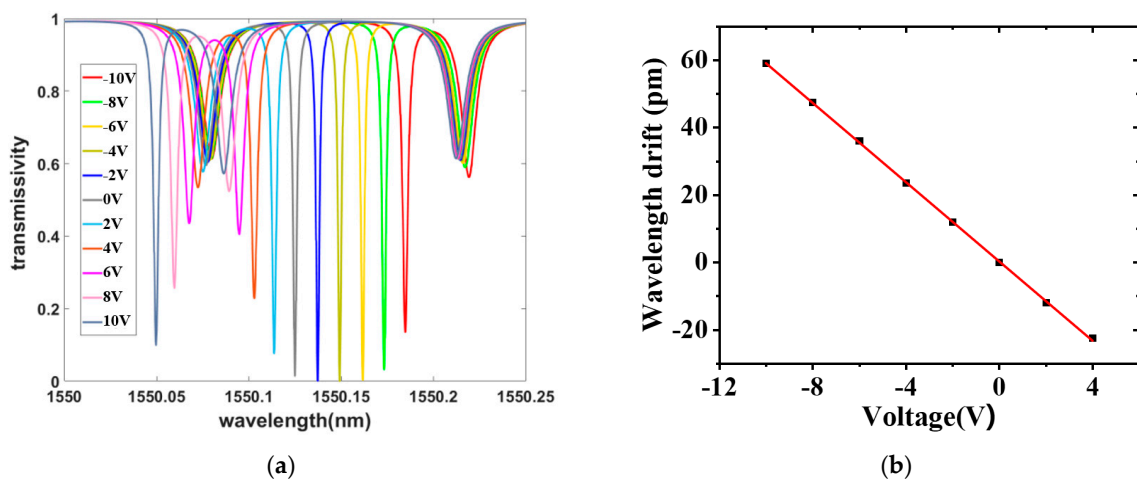


Figure 12. (a) The transmission characteristic curves of the double ring resonator at different wavelengths and applied RF signals and (b) the wavelength drift at different applied RF signals.

4. Conclusions

In summary, through the comparison and analysis of the double ring resonator and the single ring resonator, we demonstrate that the Q-factor of the double ring resonator under modulated 35 GHz RF signals is 7.05×10^8 in an ideal situation. It is improved by two orders of magnitude and can effectively improve the modulation performance of the conventional single ring resonator. In the future, the processing of the chip will be completed based on the parametric analysis of the microring structure presented in this paper in order to verify the performance of the double ring structure under 35 GHz modulation. Meanwhile, the proposed double ring resonator has certain scalability and its potential applications in microwave photonics, biosensing, and communication fields.

Author Contributions: Z.W., X.Y. and M.Z. proposed the conceptualization and methodology; Z.W. analyzed the data, reviewed and modified the manuscript; L.Z. and S.H. carried out the simulations, and wrote the original draft preparation; L.Z., S.H., H.L. and Z.W. edited and revised the article; D.L., T.W. and W.C. contributed investigation; L.G. and X.Y. contributed data analysis and modification of the paper. All authors have read and agreed to the published version of the manuscript.

Funding: This work was supported by “Dalian Life and Health Planning Project”(2022ZXYG22) and “Fundamental Research Funds for the Central Universities”(2022ZXYG22).

Institutional Review Board Statement: The study was not applicable involving humans or animals.

Informed Consent Statement: The study was not applicable involving humans or animals.

Data Availability Statement: Data available in a publicly accessible repository.

Acknowledgments: Z. Wu, L. Guo and M. Zhao would like to acknowledge the financial support from Dalian Life and Health Planning Project and Fundamental Research Funds for the Central Universities.

Conflicts of Interest: The authors declare no conflict of interest.

References

1. Law, F.K.; Uddin, M.R. Digital electro-optic exclusive OR and NOR gates utilizing a single micro-ring resonator. *Optik* **2020**, *200*, 163361. [[CrossRef](#)]
2. Pandey, A.; Jeyaselvan, V.; Selvaraja, S.K. Broadband optical single sideband generation using an ultra high shape-factor self coupled ring resonator. *Opt. Commun.* **2020**, *461*, 125224. [[CrossRef](#)]
3. Zhu, D.; Shao, L.; Yu, M.; Cheng, R.; Desiatov, B.; Xin, C.; Hu, Y.; Holzgrafe, J.; Ghosh, S.; Shams-Ansari, A. Integrated photonics on thin-film lithium niobate. *Adv. Opt. Photonics* **2021**, *13*, 242–352. [[CrossRef](#)]
4. Luan, E.; Yun, H.; Laplatine, L.; Dattner, Y.; Ratner, D.M.; Cheung, K.C.; Chrostowski, L. Enhanced sensitivity of subwavelength multibox waveguide microring resonator label-free biosensors. *IEEE J. Sel. Top. Quantum Electron.* **2018**, *25*, 1–11. [[CrossRef](#)]
5. Wan, L.; Chandralalim, H.; Chen, C.; Chen, Q.; Mei, T.; Oki, Y.; Nishimura, N.; Guo, L.J.; Fan, X. On-chip, high-sensitivity temperature sensors based on dye-doped solid-state polymer microring lasers. *Appl. Phys. Lett.* **2017**, *111*, 061109. [[CrossRef](#)]
6. Han, H.; Xiang, B. Integrated electro-optic modulators in x-cut lithium niobate thin film. *Optik* **2020**, *212*, 164691. [[CrossRef](#)]
7. Wang, C.; Zhang, M.; Stern, B.; Lipson, M.; Lončar, M. Nanophotonic lithium niobate electro-optic modulators. *Opt. Express* **2018**, *26*, 1547–1555. [[CrossRef](#)]
8. Buscaino, B.; Zhang, M.; Lončar, M.; Kahn, J.M. Design of efficient resonator-enhanced electro-optic frequency comb generators. *J. Light. Technol.* **2020**, *38*, 1400–1413. [[CrossRef](#)]
9. Dong, P. Silicon photonic integrated circuits for wavelength-division multiplexing applications. *IEEE J. Sel. Top. Quantum Electron.* **2016**, *22*, 370–378. [[CrossRef](#)]
10. Wang, S.; Feng, X.; Gao, S.; Shi, Y.; Dai, T.; Yu, H.; Tsang, H.-K.; Dai, D. On-chip reconfigurable optical add-drop multiplexer for hybrid wavelength/mode-division-multiplexing systems. *Opt. Lett.* **2017**, *42*, 2802–2805. [[CrossRef](#)]
11. Li, Z.; Guo, Z.; Li, X.; Xie, R.; Xue, H.; Bai, L.; Wang, Z. Graphene light modulator based on dual-ring resonator structure. *Opt. Quantum Electron.* **2020**, *52*, 1–12. [[CrossRef](#)]
12. Zhang, C.; Morton, P.A.; Khurgin, J.B.; Peters, J.D.; Bowers, J.E. Ultralinear heterogeneously integrated ring-assisted Mach-Zehnder interferometer modulator on silicon. *Optica* **2016**, *3*, 1483–1488. [[CrossRef](#)]
13. Ahmed, A.N.R.; Shi, S.; Zablocki, M.; Yao, P.; Prather, D.W. Tunable hybrid silicon nitride and thin-film lithium niobate electro-optic microresonator. *Opt. Lett.* **2019**, *44*, 618–621. [[CrossRef](#)] [[PubMed](#)]
14. Zhang, M.; Wang, C.; Cheng, R.; Shams-Ansari, A.; Lončar, M. Monolithic ultra-high-Q lithium niobate microring resonator. *Optica* **2017**, *4*, 1536–1537. [[CrossRef](#)]
15. Qiu, F.; Han, Y. Electro-optic polymer ring resonator modulators. *Chin. Opt. Lett.* **2021**, *19*, 041301. [[CrossRef](#)]
16. Boes, A.; Corcoran, B.; Chang, L.; Bowers, J.; Mitchell, A. Status and potential of lithium niobate on insulator (LNOI) for photonic integrated circuits. *Laser Photonics Rev.* **2018**, *12*, 1700256. [[CrossRef](#)]
17. Bahadori, M.; Yang, Y.; Goddard, L.L.; Gong, S. High performance fully etched isotropic microring resonators in thin-film lithium niobate on insulator platform. *Opt. Express* **2019**, *27*, 22025–22039. [[CrossRef](#)]
18. Cai, L.; Kong, R.; Wang, Y.; Hu, H. Channel waveguides and y-junctions in x-cut single-crystal lithium niobate thin film. *Opt. Express* **2015**, *23*, 29211–29221. [[CrossRef](#)]
19. Wang, Y.; Chen, Z.; Cai, L.; Jiang, Y.; Zhu, H.; Hu, H. Amorphous silicon-lithium niobate thin film strip-loaded waveguides. *Opt. Mater. Express* **2017**, *7*, 4018–4028. [[CrossRef](#)]
20. Jin, S.; Xu, L.; Zhang, H.; Li, Y. LiNbO₃ thin-film modulators using silicon nitride surface ridge waveguides. *IEEE Photonics Technol. Lett.* **2015**, *28*, 736–739. [[CrossRef](#)]
21. Wu, R.; Wang, M.; Xu, J.; Qi, J.; Chu, W.; Fang, Z.; Zhang, J.; Zhou, J.; Qiao, L.; Chai, Z. Long low-loss-litium niobate on insulator waveguides with sub-nanometer surface roughness. *Nanomaterials* **2018**, *8*, 910. [[CrossRef](#)] [[PubMed](#)]
22. Zhang, K.; Chen, Z.; Feng, H.; Wong, W.-H.; Pun, E.Y.-B.; Wang, C. High-Q lithium niobate microring resonators using lift-off metallic masks. *Chin. Opt. Lett.* **2021**, *19*, 060010. [[CrossRef](#)]
23. Zhou, Z.; Zhang, S. Electro-optically tunable racetrack dual microring resonator with a high quality factor based on a Lithium Niobate-on-insulator. *Opt. Commun.* **2020**, *458*, 124718. [[CrossRef](#)]

Disclaimer/Publisher’s Note: The statements, opinions and data contained in all publications are solely those of the individual author(s) and contributor(s) and not of MDPI and/or the editor(s). MDPI and/or the editor(s) disclaim responsibility for any injury to people or property resulting from any ideas, methods, instructions or products referred to in the content.